Journal of South American Earth Sciences 115 (2022) 103746

Contents lists available at ScienceDirect

Journal of South American Earth Sciences

journal homepage: www.elsevier.com/locate/jsames

Exploration of sedimentary deposits in the Atacama Desert, Chile, using integrated geophysical techniques

B. Blanco-Arrué [a,*], P. Yogeshwar [a], B. Tezkan [a], W. Mörbe [a], D. Díaz [c], B. Farah [c], S. Buske [d], L. Ninneman [d], J.P. Domagala [e], J.L. Diederich-Leicher [b], A.C. Gebhardt [f], V. Wennrich [b]

[a] University of Cologne, Institute of Geophysics and Meteorology, Pohligstrasse 3, 50969, Cologne, Germany
[b] University of Cologne, Institute of Geology and Mineralogy, Zülpicher Str.49a, 50674, Cologne, Germany
[c] University of Chile, Department of Geophysics, Blanco Encalada, 2002, Santiago, Chile
[d] Institute of Geophysics and Geoinformatics, TU Bergakademie Freiberg, Gustav-Zeuner-Strasse 12, 09599, Freiberg, Germany
[e] Servicio Nacional de Geología y Minería, Departament of General Geology, Avda. Santa María, 0104, Santiago, Chile
[f] Alfred Wegener Institute (AWI) Helmholtz Centre for Polar and Marine Research, D-27568, Bremerhaven, Germany

ARTICLE INFO

Keywords:
Transient electromagnetics
Seismics
Magnetic mapping
Electrical conductivity
Sedimentary deposits
Clay pan

ABSTRACT

The Atacama Desert is a unique landscape to understand the evolution of the Earth in extremely arid environments. Clay pans are crucial to comprehend the surface and subsurface processes in areas limited by water availability. We present an integrated geoscientific study to investigate the sedimentary deposits of the Paranal clay pan located in the hyperarid core of the Atacama Desert. We used the loop source transient electromagnetic (TEM) method complemented by magnetics and active seismics to resolve different subsurface properties at different spatial scales. A total of 116 soundings were processed, analyzed, and inverted to investigate the resistivity distribution of the clay pan. The TEM-1D inversion results reveal a three-layered resistivity structure with reliable information down to a depth of 250 m. Colluvial and lacustrine sediments reach a maximum thickness of about 160 ± 10 m. The shape of the lacustrine sediments suggests the presence of an old paleochannel that might be part of the former main Paranal drainage network. In addition, the basement below the clay pan can be partly interpreted as a damaged zone of an inferred strike-slip fault system. Subsequent 2D magnetic modeling confirms the basement depth derived from the TEM results. The seismic transects reveal accurate structural information of the upper 60 m and are consistent with TEM-1D models. High P wave velocities correlate with high electrical conductivity layers and are interpreted as lacustrine sediments. Our work provides key information with respect to the sedimentary thickness above the basement contributing to paleoclimate research in northern Chile.

1. Introduction

The Atacama Desert in northern Chile is known as one of the driest areas on Earth, characterized by scarce precipitation with a mean annual precipitation (MAP) less than 3 mm/yr (DGAC, 2019). The region provides unique opportunities to study surface and subsurface processes, which are severely and predominantly driven by the limited water availability (Houston and Hartley, 2003; Hartley et al., 2005). The patterns of surface processes and fluvial landscape evolution in the hyperarid regions both on Earth as well as on Mars provide key information to understand the desertification and the processes controlling the extreme aridity. For example, on Mars, the surface and shallow subsurface water contributed to regionally extensive erosion, sediment transport, and chemical alteration (Phillips et al., 2001; Solomon et al., 2005).

Water-driven processes in extremely water-limited environments that cover significant areas of Earth, such as the Atacama Desert, are not well understood. Studying the climate history of the Atacama Desert is crucial to better understand the controlling factors and the desertification processes. The Cenozoic climate history of hyperarid sites in the Atacama Desert has been studied during the past decades by several authors, covering different aspects, such as the chronology, climatic condition, and erosion processes (e.g., Hartley and Chong, 2002; Dunai et al., 2005; Ritter et al., 2019; Diederich et al., 2020; Dunai et al.,

---

* Corresponding author.
E-mail address: barbyra90@gmail.com (B. Blanco-Arrué).

https://doi.org/10.1016/j.jsames.2022.103746
Received 26 October 2021; Received in revised form 7 February 2022; Accepted 9 February 2022

2020). The present work contributes to an interdisciplinary research project CRC-1211 (http://sfb1211.uni-koeln.de/) seeking the mutual evolutionary relationships between Earth surface processes and biota under extreme water limitation.

Sedimentary deposits in endorheic basins, such as clay pans, are widespread along the Coastal Cordillera of the Atacama Desert and are mainly formed by drainage blocking due to past tectonic activity, which resulted in perfect sediment traps. Detecting the subsurface geometry of these clay pans provides essential insights into the depositional regimes and sedimentation rates, the uplift history, and are indirectly linked to the period in which the subsurface was exposed to different fluvial or arid periods. Some of these sedimentary deposits are sensitive archives of the Atacama paleoclimate and contain valuable information of the precipitation history (Ritter et al., 2018b; Diederich et al., 2020). One clay pan in the northern part of the Coastal Cordillera (~24.48°S and ~70.14°E, 2200 m.a.s.l.), located in the Pampa Remiendos near Cerro Paranal (in the following referred to as *Paranal site* throughout this article), intensively studied by the CRC 1211 project to recover a widely continuous climate record from the Coastal Cordillera. In addition, the sediment body of this clay pan presumably dates back to the onset of hyperaridity in the Mio-Pliocene, which makes it to a key site for paleoclimate investigations.

Electromagnetic (EM) methods are a valuable tool for geological studies and can provide a better understanding of the subsurface internal structure. These methods are widely used for example for mining exploration, environmental, hydrogeological, and geothermal studies. The loop source Transient Electromagnetic (TEM) method is an active electromagnetic method measuring the temporal decay of the induced magnetic field caused by alternating current in a wire loop transmitter laid out on the surface (Goldman and Neubauer, 1994). The transient decay of the induced eddy currents depends on the subsurface electrical resistivity structure (Spies, 1989; Nabighian and Macnae, 1991). Depending on the transmitter-receiver geometry, the subsurface resistivity and the observed time range, typically maximum depths between roughly 150 m–300 m can be sounded. The loop source TEM method is widely used for the investigation of groundwater studies and aquifer characterization (Fitterman and Stewart, 1986; Goldman and Neubauer, 1994). Moreover, this method can also provide valuable subsurface information for sedimentary basin studies in arid environments, for example sedimentary geometry as well as bedrock topography (Frischknecht and Raab, 1984; Danielsen et al., 2003; Yogeshwar et al., 2013). Recently, few case studies from Chile were presented aiming to study the hydrogeological situation for example in the Santiago Basin (Blanco-Arrué et al., 2021) or the El Tatio geothermal geyser fields (Montecinos-Cuadros et al., 2021). Other EM methods, such as deep Magnetotellurics are widely used for deep crustal studies, such as the tectonic evolution of the Andes, or deep geothermal targets (Hoffmann-Rothe et al., 2004; Reyes-Wagner et al., 2017; Cordell et al., 2018; Ślęzak et al., 2021). Other non-EM geophysical techniques, such as gravimetry and magnetics, have been commonly used to study different features in the Atacama Desert at local and regional scales (Ugalde et al., 2007; García-Pérez et al., 2018; Bascuñán et al., 2019). Geophysical methods have different resolution capabilities to resolve subsurface physical properties and often are combined to achieve optimal target resolution answering questions on different spatial scales (Díaz et al., 2014; Yáñez et al., 2020; Bücker et al., 2021).

In the present study, we integrated the results of the loop source TEM with magnetics and active seismics to resolve different subsurface properties of the Paranal site at different spatial scales. The purpose of our study is to (1) provide key information with respect to depth and morphology of the sedimentary layers as well as the basement rocks; (2) characterize the 3D geometry and internal structure of the clay pan; (3) link the results of the various geophysical models to the regional geological conditions.

2. Geological and climatological background

The Atacama Desert is known to be the driest desert on Earth and extends from southern Peru (~18°S) to northern Chile (~27°S). On a large scale, the main factors that contribute to the overall hyperaridity of the Atacama Desert are: (1) the rain shadow of the Andes to the east, blocking the moisture coming from the Atlantic Ocean (Houston and Hartley, 2003), (2) the regional position within the subtropical high-pressure belt, and (3) the upwelling of cold water to the west related to the Pacific Ocean's Humboldt current (Hartley and Chong, 2002; Houston and Hartley, 2003; Hartley et al., 2005; Clarke, 2006).

Fig. 1a shows the study area governed by the Vickuña Mackenna batholith (Herve and Marinovic, 1989). This batholith is composed of remnants of a Mesozoic magmatic arc formed at the early stage of the modern Andes due to the subduction of the oceanic Nazca plate under the continental South American plate since the Cretaceous (Pardo-Casas and Molnar, 1987). Of the six major regional intrusive units, the most prominent in the study area (Fig. 1b) are (1) the Diorite-granodiorite Cerro La Campana (Middle to Late Jurassic, 166-158 Ma), (2) Granodiorite Quebrada Grande (Late Jurassic, 157 Ma) (3) the Ventarrones plutonic complex (Late Jurassic to Early Cretaceous, 149-138 Ma), and (4) the Remiendos plutonic complex (Early Cretaceous, ca. 135 Ma) (Domagala et al., 2016). During the Late Oligocene to Early Miocene, the region was filled up by volcanoclastic sediments (Coira et al., 1982; Mpodozis and Ramos, 1990; Carrizo et al., 2008).

Clay pans are widespread along the Coastal Cordillera in northern Chile and are mainly filled with clastic sediments. The Paranal site is located in the center of the Pampa Remiendos (~24°S and ~70°E) at an elevation of about 2200 m.a.s.l. (Fig. 1b). The modern clay pan (highlighted in red in Fig. 1d) is oriented in the southeast direction. Three hills surround the study area: Ventarrones (2622 m.a.s.l.), Armazones (3064 m.a.s.l.), and Vicuña Mackenna (3114 m.a.s.l.). The last two are part of the so-called Sierra Vicuña Mackenna (Herve and Marinovic, 1989; Marinovic et al., 1995).

The Paranal site is placed in the middle of the Pampa Remiendos unit, which comprises Miocene to Pliocene with variable thickness as well as variable degrees of sediment compaction and grain size. The formation of the basin is linked to tectonic blocking as part of a large-scale east-southeast and west-northwest trending drainage system described by Scheuber and Andriessen (1990) (highlighted in dashed light blue in Fig. 1a). According to Herve (1987), the vertical movements of the Atacama Fault Zone (AFZ) took place between 5.5 and 19 Ma (e.g. Paposo Fault), suggesting the existence of this paleochannel system since the pre-late Miocene (Marinovic et al., 1995).

Currently, no information about the thickness of the sediment infill or the basement depth of the Paranal clay pan exists, making it one major focus of this paper. However, some constraints on the sediment succession of the Paranal site can be drawn from an intensive drilling campaign of another clay pan (PAG site, 250 km to the north of Antofagasta city) in the central Atacama which exhibits similar tectonic formations. The drilling operation that was conducted in 2017 within the CRC-1211 project recovered sediment information down to a depth of 52 m (Diederich-Leicher, 2020; Dunai et al., 2020).

The Quebrada Grande Fault System (QGFS) crosses the study area from north to south and are part of the AFZ (Herve, 1987; Scheuber and Andriessen, 1990). The QGFS corresponds to a left-lateral strike-slip fault with an extension of 55 km in north-south direction. Based on the

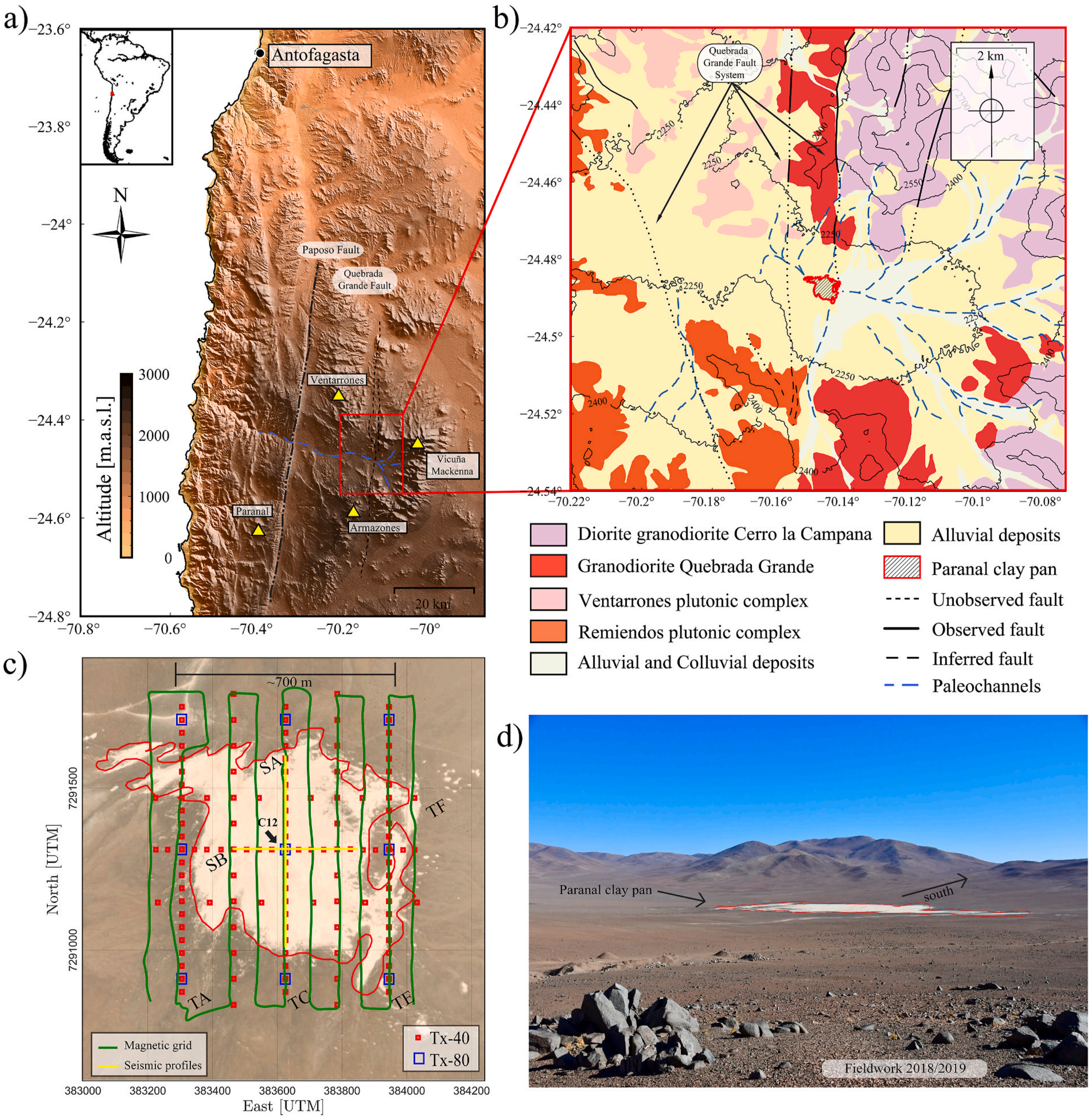

Fig. 1. (a) Location of the study area (NASA, 2020). The highest hills around the study area are marked with yellow triangles. The red square highlights the studied geology. (b) Geological context of the Paranal site (Domagala et al., 2016). The lithology and the main intrusives and plutonic complexes are describe in the legend below. Isolines describe the elevation in m.a.s.l. (c) Geophysical survey layout. The TEM soundings in red and blue squares correspond to Tx-40 and Tx-80 setup, respectively. Two Seismic profiles in yellow (SA - north-south and SB - east-west). The magnetic grid is shown in green. TEM profiles TA, TC, TE and TF are also illustrated. Map data: ESRI satellite image. (d) Picture oriented towards the southeast direction. (For interpretation of the references to color in this figure legend, the reader is referred to the Web version of this article.)

geology, the Granodiorite Quebrada Grande is placed near the fault system (Late Jurassic, ca. 157 Ma), and its inferred surface trace is shown in Fig. 1b (Domagala et al., 2016). Inside the clay pan and its vicinity, the fault is covered by colluvial and alluvial sediments (Fig. 1b).

Several studies reveal the existence of mylonites with a sense of sinistral movement (Scheuber and Andriessen, 1990; Brown et al., 1993) suggesting a Late Jurassic (156–159 Ma) age of deformation. However, studies of minor north-northeast oriented faults reveal that the subsystem of the Quebrada Grande faults does not exhibit deformation in the Earlier Cretaceous plutons of the Patches Plutonic Complex, indicating the movements to be of Late Jurassic to Early Cretaceous age (Herve and Marinovic, 1989; Álvarez et al., 2016).

The main formations prospected using applied geophysics within the Paranal clay pan are different sediments layers that cover the area and the deposits placed beneath. It should be pointed out that the clay pan is in an area where it crosses the QGFS and the exact location of the trace at depth is unknown (Fig. 1b).

3. Geophysical surveys

3.1. Transient electromagnetic

The TEM measurements were carried out on a 3D grid with a total amount of 116 soundings covering the entire surface of the clay pan. The data acquisition took place during two surveys in October 2018 and December 2019. The soundings were performed utilizing the WalkTEM device (ABEM, 2016). This device provides two acquisition modes depending on the required exploration depth: Low Moment (LM) with low current (~2 A) at a high transmitter cycle frequency (~222 Hz) for acquiring early time data, and High Moment (HM) with high current (~11 A) and low cycle frequency (~25 Hz) with a longer off-times for recording late time data and deep subsurface imaging. Additionally, electromagnetic noise was measured at each station.

TEM can be carried out utilizing different configurations (Nabighian and Macnae, 1991). On this work, the soundings were carried out using a central-loop configuration, with an outer loop as a transmitter and an inner loop as a receiver. The receiver coil Rc-200 had a loop side of 10 m with two turns to gather high quality at late times data and an amplitude gain factor of 7 (ABEM, 2016). Two different transmitter loop sizes were used: one of 40 × 40 m^2 (Tx-40) and the other of 80 × 80 m^2 (Tx-80). The profile TC and TF are considered as the main transects through the clay pan. TC is placed in north-south direction and, had a total length of 960 m with a total amount of 23 soundings, and TF, located in west-east direction, with a total length of 800 m and in total 11 soundings (Fig. 1c).

3.2. Active seismic

The seismic survey was carried out in November 2018. The objective of the seismic survey was to obtain a subsurface P wave velocity model with a higher spatial resolution for the shallow parts of the subsurface compared to TEM. Moreover, TEM has a limited resolution in the shallow subsurface and does not necessarily resolve structural changes. Fig. 1c shows the measured seismic transects SA (north-south) and SB (west-east). The seismic source consisted of an accelerated weight drop with a mass of ~40 kg and a length between 36 and 43 cm attached to a pickup truck. The weight drop was preferred because of its higher emitted energy compared to a conventional sledgehammer source. Shorter source-receiver distances were used at the center of the clay pan in order to increase the spatial resolution at shallow depths. Information on the shallow structure is required for the correct subsequent analysis of the deeper seismic data. The total length of the profile SA is approximately 576 m and was acquired using 288 vertical-component geophones as receivers. The profile SB is approximately 384 m long and comprises 192 geophones. The spacing of source points was 2 m in the central part and 4 m at the boundary of the clay pan.

3.3. Magnetics

To complement TEM and seismic measurements, a magnetic survey in the Paranal site was carried out during December 2019. The aim was to obtain independent information regarding the basement structure at the study site, the subsurface extent of the clay pan sediments as well as other features, such as possible fault zones. Measurements were carried out along a grid covering the clay pan area (Fig. 1c) using an Overhauser magnetometer, with a sampling frequency of 1 Hz. A Proton precession base magnetometer with a sampling rate of 30 s was installed at the periphery of the clay pan. The base station was located in the surrounding of the clay pan during the entire measurements. The total magnetic line is about 10 km, and it was measured in north-south lines direction covering the Paranal site (Fig. 1c).

4. Results

4.1. TEM processing and 1D inversion

The TEM data are transformed from induced voltages (U_{ind}) into late-time apparent resistivities (ρ_a) in order to obtain a first impression of the conductivity distribution of the subsurface (Ward and Hohmann, 1988). The processed transients exhibit an overall high data quality within the acquired time range of two to three decades. As an example, Fig. 2 shows the induced voltage and late time apparent resistivity of sounding C12 using the Tx-40 and Tx-80 transmitter size (seen in Fig. 1c). Both obtained transients using the Tx-40 and Tx-80 setup are consistent. The stacked noise level is plotted to estimate to which limit the data is useful. A rather low noise level is visible in all measurements, which is expected due to the scarcity of anthropogenic noise sources in the study site. An average induced voltage level of $\eta = 3\times 10^{-10}$ V/Am^2 at $t = 2 \times 10^{-3}$ s is observed at all stations (Fig. 2a). It should be pointed out that the Tx-80 setup provides a larger depth of investigation (DOI) due to the increased transmitter moment and higher signal-to-noise ratio (Fig. 2a). However, the late time data for both transmitter setups clearly indicate a resistivity increase at depth (around $t = 1 \times 10^{-3}$ s in Fig. 2b). Due logistics and higher survey speed, we chose the Tx-40 setup and used the larger loop only at a few control points.

Two different 1D inversion techniques were used to analyze the processed data: The damped Marquardt-Levenberg technique (Menke, 2018; Scholl, 2005), and a multi-layered Occam smooth models which use a first-order (R1) smoothness constraint functional for the objective function (Constable et al., 1987). The uncertainties of the models are derived using equivalent models (Menke, 2018; Yogeshwar et al., 2020). The total estimated measurement errors are around 3%, which is a suitable range for an error weighted inversion. The DOI was calculated for each 1D mode2l to obtain the depth in which our model is reliable using the empirical estimation suggested by Meju (1998):

$$\delta_{doi} = \frac{\sqrt{2t\overline{\rho}/\mu_0}}{2.3}, \tag{1}$$

with t being the last transient time, μ_0 the magnetic permeability of free space, and $\overline{\rho}$ the average resistivity of the overlying subsurface.

The global data misfit (χ) for each sounding is calculated according to

$$\chi = \sqrt{\frac{1}{N}\sum_{i=1}^{N}\left(\frac{d_{i,obs} - d_{i,calc}}{\Delta d_{i,obs}}\right)^2}, \tag{2}$$

with $d_{i,obs}$ being the observed data and $d_{i,calc}$ is the calculated data. The $\Delta d_{i,obs}$ are the measurement errors and N the number of data points. A $\chi \approx 1$ corresponds to an optimal data fit within the assumed error level.

Fig. 3 shows the TEM-1D inversion result for station C12. These derived 1D models lead to a three-layer model. A ~50 m thick more

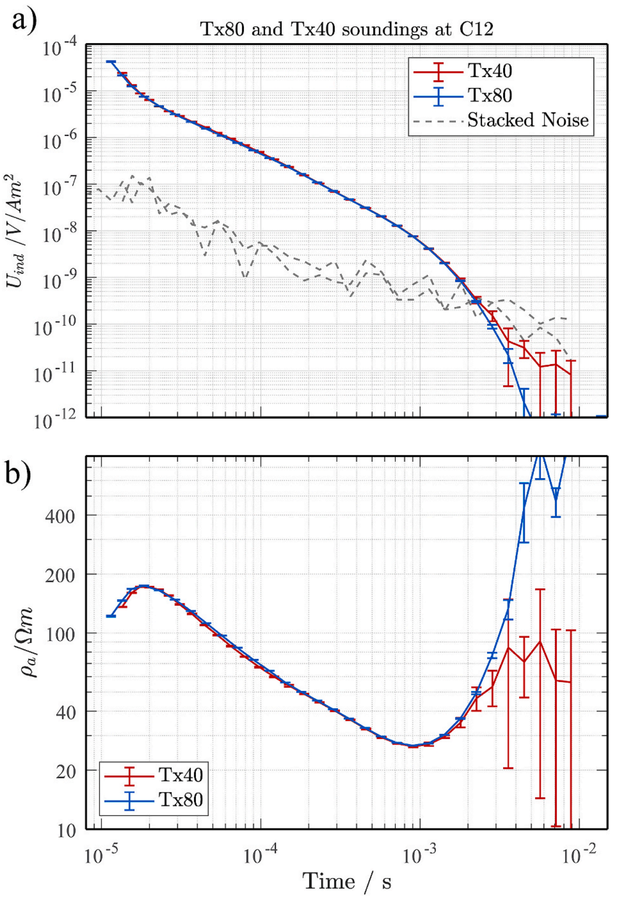

Fig. 2. Soundings with the Tx-40 and Tx-80 at station C12 of profile TC. (a) The induced voltage (U_{ind}) and (b) late-time apparent resistivity (ρ_a). The stacked noise level of each sounding is plotted as dashed grey line.

resistive ~100 Ω-m layer is followed by a conductive second layer of about 20 Ω-m and a resistive basement layer with 400 Ω-m at around 160 ± 10 m depth. The equivalent models indicate high resolution for the first and second layer. For the resistive base layer, larger uncertainties are observed. Both, Occam and Marquardt inversion results are consistent. Fig. 3b shows the data and fitting. The data is slightly under-fitted with $\chi \approx 1.3$ and $\chi \approx 2.1$ for Marquardt and Occam R1 models.

Fig. 4a and b shows the stitched 1D Occam R1 inversion results along the profiles TC and TF. In addition, the uncertainty of the base layer depth is calculated from the equivalence models and shown as a vertical error bar for each model. The resistivity distribution of the clay pan can be interpreted by a three-layered structure. Both profiles illustrate a first layer with a high resistivity greater than 100 Ω-m, roughly 50 m thick. The resistive layer is followed by a second conductive layer of roughly 20 Ω-m. A more resistive base layer with ~200 Ω-m is present. For both profiles, the DOI can be seen below 2000 m.a.s.l., suggesting reliable models down to ~250 m depth.

For better visualization, the profile TC is divided into three zones (Z1, Z2, and Z3), where the profile TF transect is the perpendicular zone Z2. The zones Z1 and Z3 represent the edges of TC with a reduced thickness of the conductor. The shape of the conductive body along Z2 extends in a west-east orientation and has a rather homogenous depth (Fig. 4a and b). In the same manner, in a north-south orientation, the profile TC exhibits a clear channel-like shape the center. The equivalent models derived below each station, indicate a depth variability of 11 m for the base layer.

Slightly different slopes angles of the base ranging from 13° to 20° at both sides can be inferred. The global data misfit for profile TC and TF is almost optimal with $\chi \approx 1.2$ and 1.4 (Fig. 4c). For profile TC a slightly reduced fit is overserved in the central part. It should be noted that the derived 1D models along profile TC show a pant leg shaped conductivity increase within the basement layer towards both sides of the conductive anomaly (Fig. 4a). This can be due to multidimensional effects and are discussed further below in section 4.2.

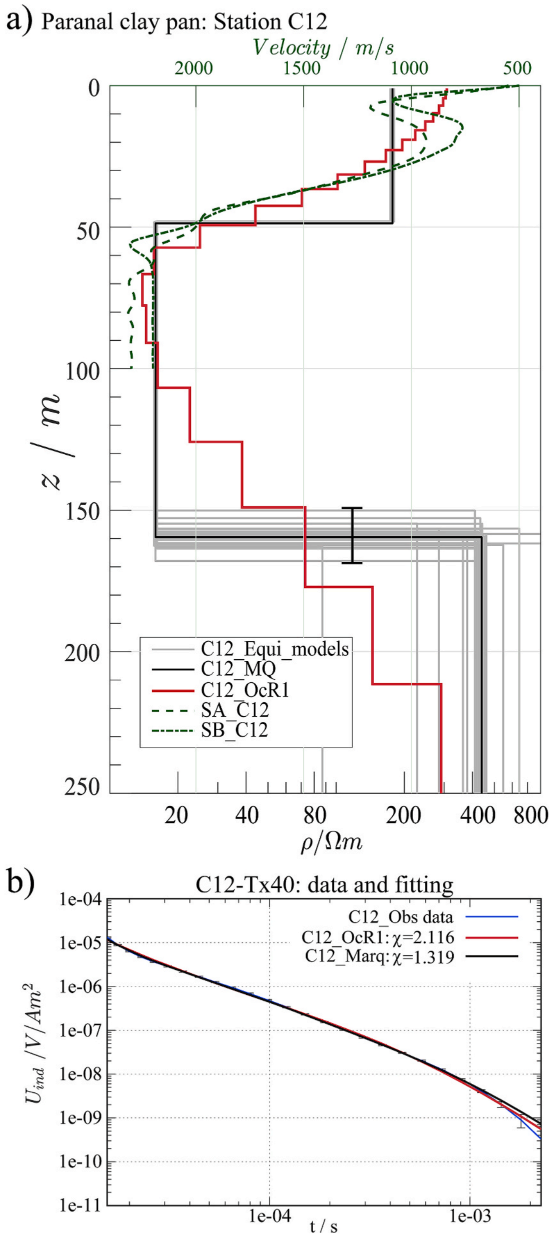

Fig. 3. (a) Marquardt, Occam R1 and the equivalent 1D models for station C12 at Paranal site. The error bar shows the variation in meters of the depth by the equivalent models at station C12. SA_C12 and SB_C12 are the velocity-depth curves derived by the tomography results of seismic profiles SA and SB at same location of station C12. (b) Observed and calculated TEM data for each inversion approach.

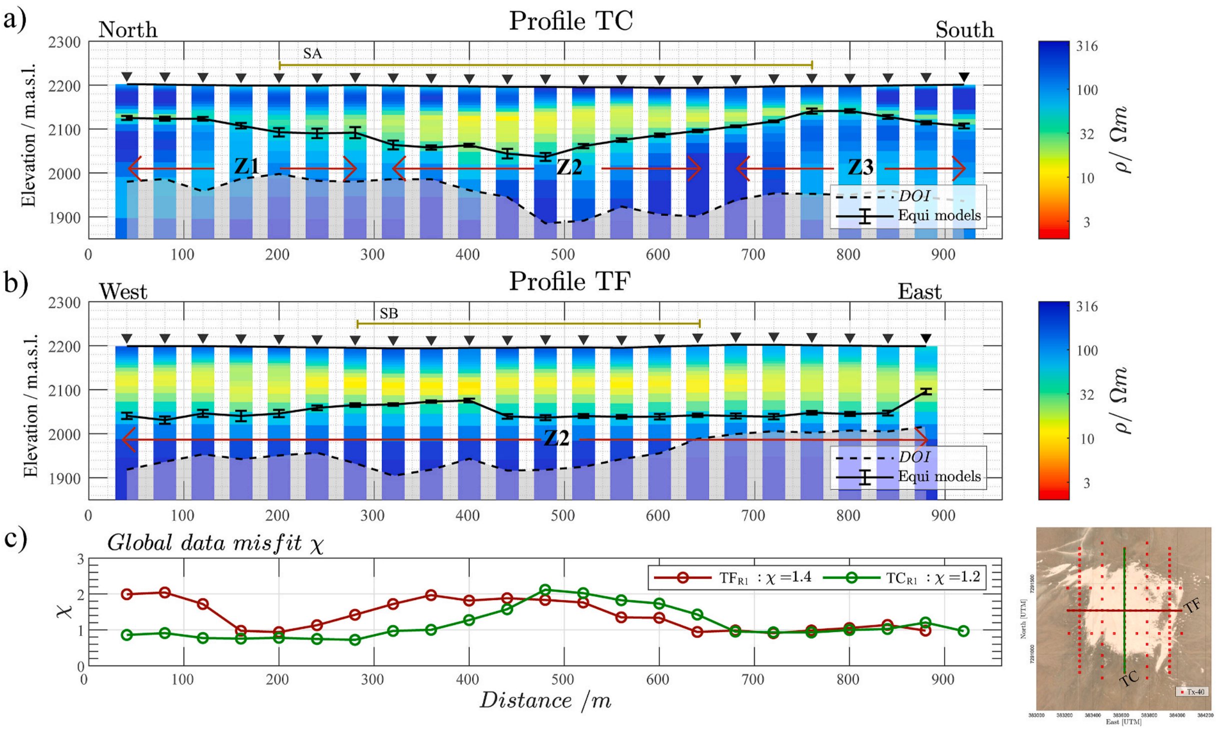

Fig. 4. 1D stitched inversion results using Occam R1 models for profile (a) TC and (b) TF. Stations are illustrated by black triangles. The DOI is plotted as a dashed line. The depth of the basement obtained by the equivalent models are displayed as error bars. The location of seismic profiles SA and SB are highlighted above the stations. Zones Z1, Z2 and Z3 are marked along the profile. (c) Global data misfit χ along the profiles.

4.2. Estimating 2D effects in the TEM data

In cases, where the subsurface is not 1D layered, multidimensional effects can lead to false interpretations of TEM data. As the electromagnetic fields diffuse faster in a resistive environment and are decelerated in a conductor, lateral subsurface variations cause distortion of the electromagnetic fields (Sudha et al., 2011; Yogeshwar and Tezkan, 2018). Although no clear distortion effects are visible in the Paranal TEM-sounding data, the derived resistivity distribution along the quasi 2D profiles might be influenced. To validate the reliability of our 1D interpretation and to check if our data is affected by 2D distortion effects, we perform a simple 2D modeling study.

The 2D TEM forward modeling utilizes the time-domain finite-difference algorithm SLDMem3t (Druskin and Knizhnerman, 1988, 1994; Druskin et al., 1999). The algorithm has been successfully applied to a variety of loop source TEM modeling studies in 2D/3D (Hördt et al., 1992; Martin, 2009; Sudha et al., 2011; Rödder and Tezkan, 2013; Yogeshwar and Tezkan, 2018; Montecinos-Cuadros et al., 2021).The algorithm uses a material averaging scheme that basically decouples the model from the finite-difference grid. In our case, the grid typically has dimensions of the order 2875 cells. The transmitter loop is set up on cell edges and is basically formed by the superposition of several dipoles forming a loop source. The electric fields are calculated on edges and magnetic fields on cell faces. An exact boundary condition is used at the air-earth interface. A Krylov subspace method is used to solve the induction equation in three dimensions with rather few computational requirements. For further details, we refer to the above articles.

Fig. 5a shows the derived 1D models using the Marquardt inversion technique for the profile TC (Fig. 1c). The variation of the basement depth derived by the equivalence models is illustrated as an error bar for each model. Based on the 1D inversion results of field data, we generated a 2D model by interpolating the 1D models of each station (shown in Fig. 5b). The same zones described in Fig. 4a are sketched for comparison. As stated earlier, the derived 1D models along profile TC show a pant leg shape conductivity increase within the base layer towards both side of the conductive anomaly, which might indicate a 2D effect.

The derived error weighted relative difference between the forward 2D and 1D model response is termed as χ_d , given by

$$\chi_d = \frac{F(m)_{2D\_}F(m)_{1D}}{\delta F(m)_{2D}}, \tag{5}$$

and is illustrated as a pseudo section in Fig. 5c. The χ_d section shows a deteriorated fit that partly correlates with the subsurface structure of the clay pan. A high deteriorated fit is observed at earlier times towards the edges of the clay pan and at late time in the central part. The global error-weighted fit of the 2D and the 1D synthetic response is about $\chi_d = 2.0$. The deteriorated fit observed partly in zone Z1, Z2 and until midway of zone Z3 is obviously associated with 2D distortion effects. A reason is the large slope angle of the basement towards the edges of the clay pan. As a consequence, the depth of the basement might be slightly underestimated using the 1D inversion approach due to the 2D effects of both clay pan slope angles.

To simply test this hypothesis, we generated a new slightly altered 2D model and applied the following changes: (1) a homogeneous resistivity of about 200 Ω-m was used for the third layer; and (2) the depth of the basement in zone Z2 was increased by around ~20 m in the central part (Fig. 5d). Fig. 5e illustrates the data misfit for each sounding along the profile obtained by (1) the original 1D inversions in Fig. 5a; (2) the 2D model derived from the 1D models in Fig. 5b, and (3) the modified 2D model in Fig. 5d. The global data misfit for the 1D models is almost optimal with $\chi = 1.2$. However, a slightly deteriorated fit is observed in zone Z2. The global data misfit for the 2D model is much higher with $\chi = 2.5$. Several stations in zone Z1 and Z3 are not well fitted. When changing the 2D model, the global data misfit improves to $\chi = 1.7$, which is not optimal but significantly improved.

The depth of the basement obtained by the 1D models and the modified 2D model varies by around 24 m in the central zone Z2 (Fig. 5f), indicating a thicker conductive body. Conclusively, our derived 1D models are overall very consistent, but the depth of the basement might be slightly underestimated when using a 1D interpretation. For an

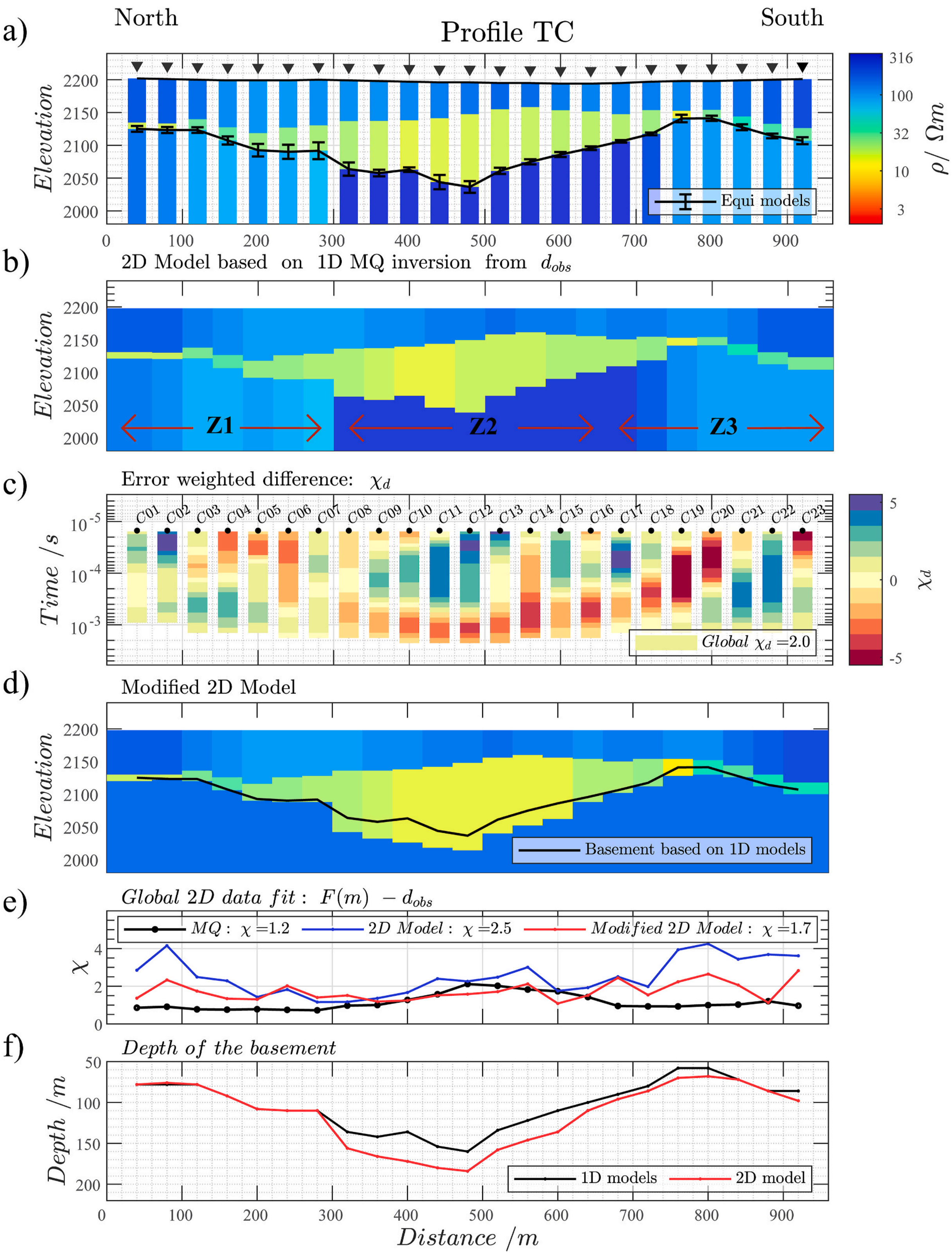

Fig. 5. (a) Stitched 1D inversion results using MQ approach for profile TC. The depth for the basement obtained by the equivalent models are displayed as error bars. Stations are illustrated by inverted black triangles. (b) 2D model generated by interpolating the obtained profile TC using MQ technique. Zones Z1, Z2 and Z3 are highlighted along the profile. (c) 2D-1D Model fitting: error weighted relative differences (χ_d) calculated from the 2D model response $F(m)_{2D}$ and the 1D model response $F(m)_{1D}$, see Eqn 5. (d) Modified 2D model with a thicker conductive layer in the center and equal basement resistivity of about 250 Ω-m. The basement depth obtained by the 1D MQ models is displayed as black line. (e) Global 2D data fit of the derived 1D models, the 2D model and the modified 2D model. (f) Basement depth of the 1D MQ models (black line) and the modified 2D model (red line).

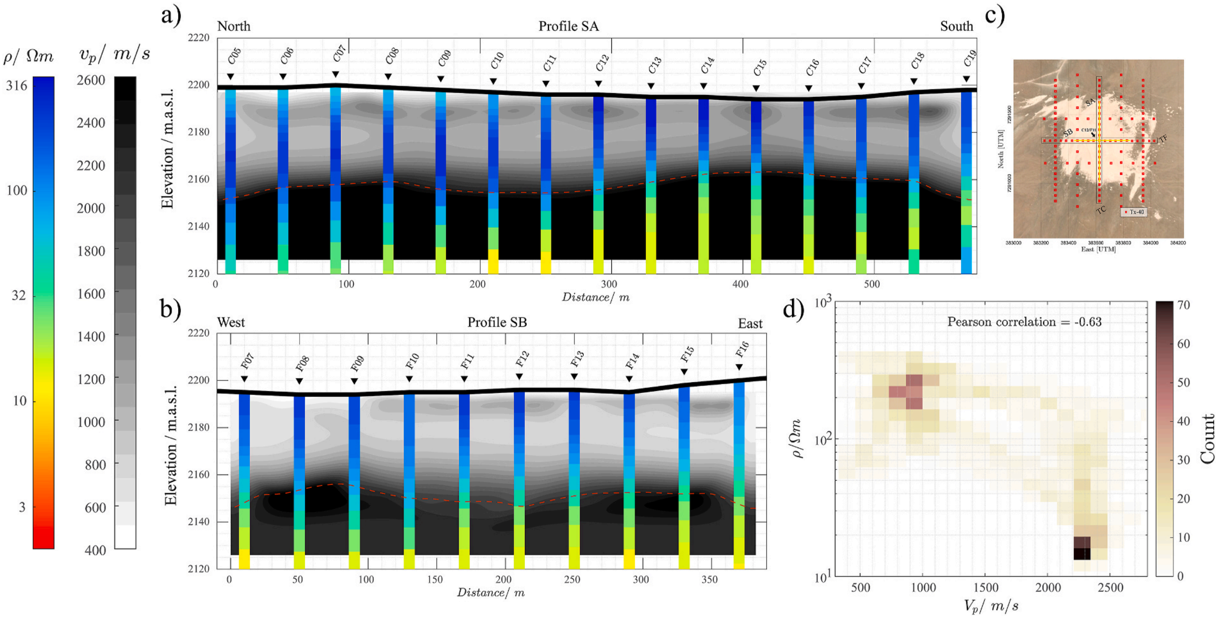

Fig. 6. P wave velocity model for profiles SA (a) and SB (b). The TEM-1D models using Occam R1 for profiles TC (a) and TF (b) are overlapped. The color bars for velocity and resistivity are displayed on the left side. Seismic isoline at 1600 m/s is shown in yellow line for each profile. (c) Map location of profiles SA and SB at Paranal site. The crossing point at station C12/F11 is highlighted in the center. d) Resistivity ρ versus velocity v_p values.

unbiased and independent interpretation, a 2D or even 3D inversion is required.

4.3. Seismic tomography inversion

After data acquisition, the P wave velocity models has been derived by seismic first-arrival travel time tomography. The used software TomoPlus (GeoTomCG) employs a nonlinear refraction travel time tomography implementation which minimizes the misfits of the average slownesses (travel times divided by ray lengths) and the apparent slownesses (travel time derivatives with respect to distance), constrained with a Tikhonov regularization (Zhang and Toksöz, 1998). Fig. 6 shows the seismic tomography results for profiles SA and SB (Ninnemann, 2020). The maximum depth of investigation z_{max} can be estimated to be about a quarter of the spread length (Frei and Keller, 2000). However, this approximation is just a rough estimate. The depth of investigation along profiles SA and SB varies between 60 and 70 m. The TEM-1D models are plotted for comparison. Fig. 6c shows the location of profiles SA and SB on a map as reference. Along both profiles a strong contrast of velocity values is observed around ~2160 m.a.s.l. The seismic isoline at 1600 m/s is highlighted as a red dashed line in Fig. 6a and b. Compared with the TEM-1D models of each profile, we observe a strong contrast in both physical parameters highlighted along the seismic isoline. The resistivity and seismic P wave velocity models are consistent and give us a clear transition between two layers.

To directly relate the velocity v_p to the resistivity ρ, from both profiles, we considered the velocity and resistivity from each sounding location. In Fig. 6d, the physical parameters are plotted against each other. Its recurrence was counted in a range of 20 units for each physical parameter. The higher the counts, the more often a resistivity–velocity pair occurs. We observe two main clusters in Fig. 6d, the overall Pearson correlation coefficient (Pearson, 1895) between the velocity and the resistivity models is −0.63 indicating a higher negative correlation. Here, higher velocities correlate with lower resistivities. Similarly, from the correlation comparison between both physical parameters, two different clusters are observed.

4.4. Lithological assumption based of the TEM data

As mentioned before, no direct lithological information about the sediment succession of the Paranal site is available. Nevertheless, some lithological information can be derived from another clay pan, previously studied within the CRC 1211 project (Ritter et al., 2018b, 2019; Diederich et al., 2020; Dunai et al., 2020). The PAG clay pan, is located near Rio Loa canyon, 250 km to the north of Antofagasta city. Similar to the Paranal site, the PAG clay pan was formed by tectonic drainage displacement due to reverse faulting of the Adamito or Aguirre Fault (Skarmeta and Marinovic, 1981; Allmendinger et al., 2005). In 2017, a deep drilling campaign was performed to study the climatic history of the Atacama Desert throughout the late Cenozoic (Diederich-Leicher, 2020; Dunai et al., 2020).

The recovered sediment sequence reveals key sediment information summarized as colluvial sediments of the uppermost 30 m underlain by lacustrine sediments down to the base at 52 m depth (Fig. 7a). More detailed descriptions about the PAG clay pan as well as core analysis can be found in Dunai et al. (2020); Ritter et al. (2019) and Diederich-Leicher (2020). In addition to the drilling, an intensive TEM and active seismic survey was carried out at the PAG site, e.g., crossing the drilling location. Whole-core Non-Contact Resistivity (NCR) data of the sediments recorded by Multi-Sensor Core Logging (MSCL; Geotek Ltd.) was used for comparison and validation of the TEM data. The bulk NCR data (blue curve) exhibit a clear contrast at a depth of 30 m that well coincides with the shift in derived resistivity of the TEM-1D model at station P1 in the center of PAG (Fig. 7a). Simultaneously, the seismic velocity increases to >1500 m/s below 20–30 m depth. This strong contrast shown by all the techniques corresponds to the transition from colluvial to lacustrine sediments as seen in the lithology of the drill core (Fig. 7a). Variations in the seismic velocity observed at shallow depths can thereby be explained by changes in the grain-size distribution of the different lithologies (clay and silt in lacustrine vs. sand and gravel in colluvial strata). Moreover, the porosity of the different sediments, e.g., due to compaction, might play a key role that influence the value of the parameters that we observe in both resistivity and velocity.

As indicated above, the TEM-1D model derived at station C12 illustrate a first and second layer resistivities of about 100 and 20 Ω-m, and with thickness roughly 50 ± 2 and 160 ± 10 m. Velocity-depth curves at

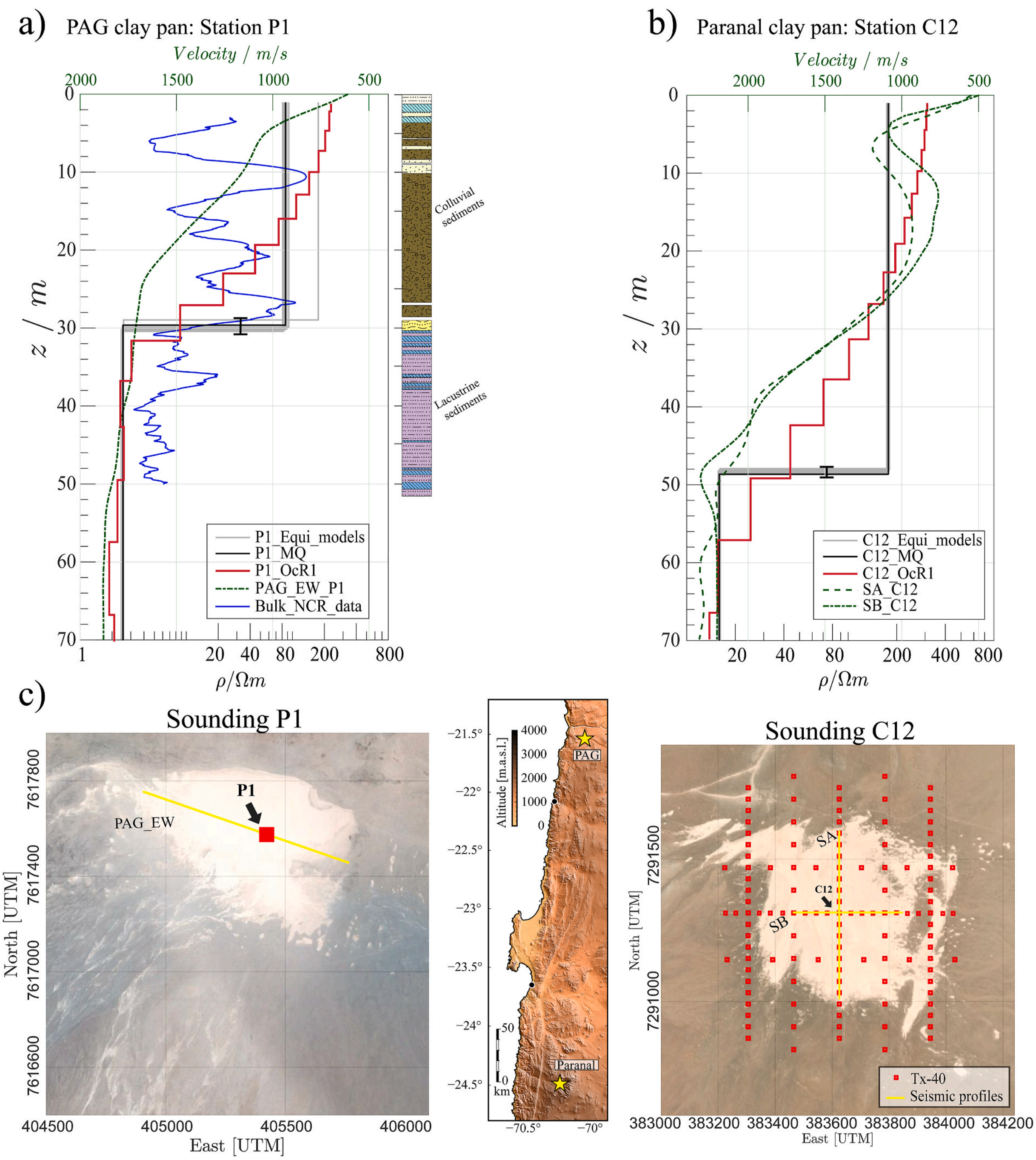

Fig. 7. Comparison of shallow-depth TEM-1D models of Occam (red line), Marquardt (black line), and velocity-depth curves from P wave seismic models (green dashed lines) for (a) Station P1 in the center of the PAG site next to lithology and non-contact resistivity (NCR; blue line) of the PAG drill core (Diederich-Leicher, 2020; Dunai et al., 2020), and (b) Station C12 at the Paranal site (TEM-1D model up to 70 m). (c) Plan view map of PAG and Paranal clay pans is shown, with the location of each station with the seismic profiles. In between, a regional location of both sites is shown. The distance between both sites is around 320 km.

site C12 exhibit three key characteristics: (1) at shallow depths (0–5 m), a velocity increase from 500 to 1100 m/s is visible; (2) a low-velocity zone about ~750 m/s exists below 10–20 m depth; (3) higher velocities >2000 m/s are observed below 50 m depth (Figs. 3 and 5).

Based on the observation from the PAG site, we can make the following assumptions for the sediment succession of the Paranal site: (1) The derived resistivities and seismic velocities of the uppermost layer are similar, suggesting colluvial sediments with similar electrical properties, underlain by low-resistivity and high-velocity lacustrine strata; (2) the transition zone between the colluvial and the lacustrine sediments at the Paranal site is roughly 20 m deeper at the center of the clay pan; (3) the resistivity of lacustrine sediments at the Paranal site is ~20 Ω-m higher than at PAG clay pan.

4.5. Magnetic anomaly at Paranal site

The magnetic data processing was performed with the Oasis Montaj software (SEEQUENT, 2021). For processing, diurnal variations and the international geomagnetic reference field (IGRF) were taken into account. The total magnetic field strength of the area is roughly 22,800 nT. A value of 23.43° and −3.82° was used for inclination and declination, respectively. The magnetic anomaly of the total field was obtained by subtracting the IGRF from each point, according to its latitude, longitude, altitude, date, and measurement time. Subsequently, to eliminate spikes and outliers, a moving window was applied in order to obtain an adequate magnetic anomaly of the total field.

To better understand the magnetic data, two conventional filter techniques were used: the Reduction to The Pole (RTP) and the Analytic Signal (AS). The RTP is used to identify the correct location of magnetic anomalies in the area (Ibraheem et al., 2018). The RTP removes the effect of induced magnetization and strike while preserving dip information. Positive anomalies indicate the position of magnetic sources, assuming the magnetization occurs in the same direction as the Earth's magnetic field. However, if the bodies have remanent magnetism, this process may present unsuitable results (Aina, 1986). The AS filter can be calculated as the square root of the sum of squares of the derivatives in the x, y, and z directions (Marson and Klingele, 1993):

$$|AS(x,y)| = \sqrt{\left(\frac{\partial M}{\partial x}\right)^2 + \left(\frac{\partial M}{\partial y}\right)^2 + \left(\frac{\partial M}{\partial z}\right)^2}, \tag{3}$$

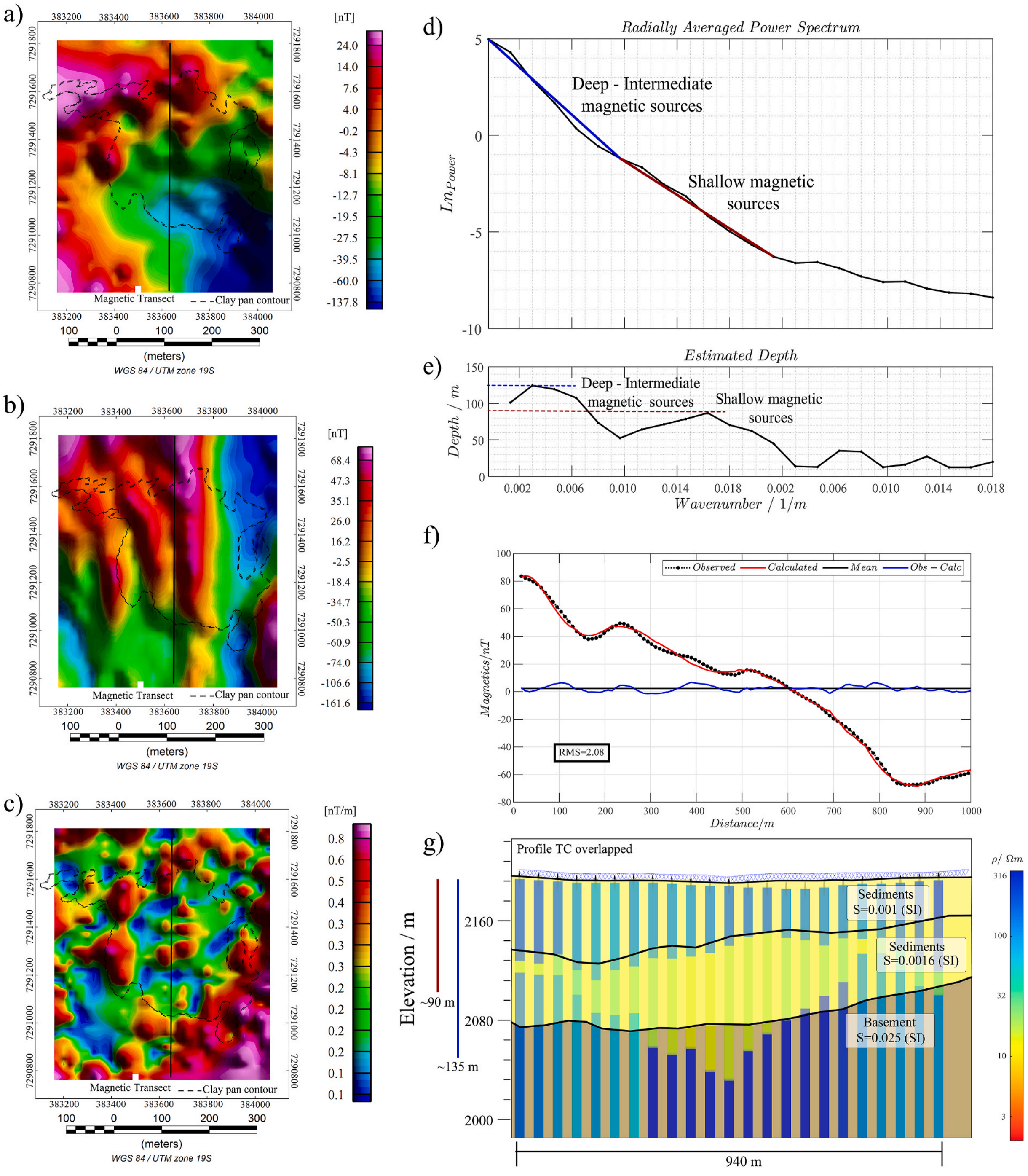

Fig. 8. Maps of (a) the Magnetic Anomaly (nT), (b) the RTP, and (c) AS response of the Paranal site. The black line corresponds to the transect on which the 2D forward modeling was derived. The clay pan boundary is shown in dashed black line. (d) 2D radially averaged power spectrum curve. The trend of the Deep-Intermediate and Shallow magnetics sources are highlighted in blue and red lines, respectively. (e) Estimated depth of the Deep-Intermediate and Shallow magnetic sources. (f) Forward modeling of the magnetic data, observed and calculated magnetic transect at the same location of profile TC (Fig. 1c). (g) 2D model of the RTP response at the magnetic transect. The TEM-1D models of profile TC using Marquardt technique are overlapped. More detail description can be found in Fig. 4.

where $|AS(x,y)|$ is the amplitude of the analytic signal at (x,y), M is the observed magnetic field at (x,y), and $\frac{\partial M}{\partial z}$ is the vertical first-order derivatives of the observed field.

The AS technique is applied to determine the magnetic source geometry (Roest et al., 1992). The AS enhances short wave length and therefore the resolution of shallow bodies while decreasing the resolution of deeper sources (Rajagopalan, 2003).

In addition, the Radially Averaged Power Spectra (RAPS) was calculated to estimate the depth of magnetic sources. The following expression suggested by Spector and Grant (1970) determines the depth of the magnetic sources:

$$h = \frac{S}{4\pi}, \tag{4}$$

where h is the depth and S is the slope of the logarithmic energy spectrum.

In a subsequent step, a 2D forward modeling was performed using the package GM-SYS available in Geosoft Oasis Montaj software (SEEQUENT, 2021). The used techniques are well described by few authors (Talwani, 1964; Won and Bevis, 1987). The used magnetic susceptibility ranges are consistent with those of published values (Ishihara and Ulriksen, 1980; Clark and Emerson, 1991).

Fig. 8 summarizes the results of the magnetic survey with the (a) magnetic anomaly field, (b) the RTP response, and (c) the AS response derived from the magnetic data. As well as (d) the RAPS result of the magnetic data and (e) the estimated depth of the main magnetic sources. From these results, it is possible to derive some qualitative interpretation:

1. A positive magnetic anomaly is observed at the western side of the study area, whereas a negative anomaly can be seen to the southeast of the clay pan (Fig. 8a, b, and 9a). The boundary between both anomalies coincides with the inferred position of one trace of the QGFS.
2. A similar signature is derived by the RTP response (Figs. 8b and 9a). Due to the RTP procedure, which locates the magnetic anomalies above the causative bodies, assuming a remanent magnetism smaller than the induced magnetism, we observed a positive anomaly towards the northwest of the clay pan. The positive magnetic anomaly and RTP response are consistent with the main intrusive rocks of the study zone (Fig. 8a, b and 9a) with a greater proximity to where they should be located the Granodiorite Quebrada Grande and part of the Ventarrones plutonic complex (see Fig. 1b).
3. From the AS response, some shallow magnetic sources are visible within the clay pan. However, higher AS values are well matching the clay pan border (Fig. 8c).
4. The RAPS technique in Fig. 8d yields two clear regions where the curve follows roughly a power law. The depth estimates for deep to intermediate and for shallow depths are roughly ~135 and ~90 m, respectively (Fig. 8e). These values coincide well with the depth of the sedimentary units derived from the TEM-1D models (Fig. 8g).

Fig. 8f and g shows the 2D forward modeling results of the RTP magnetic transect using the RTP response overlapped with the TEM-1D inversion results of profile TC. On the left side, the estimated depths by the RAPS techniques are shown (Fig. 8f). Similar to the TEM-1D models of Profile TC, the 2D magnetic model indicates a three-layer 2D model of the subsurface. The sediments are modeled with a very low magnetic susceptibility value (~0.001 SI) followed by a base layer with high magnetic susceptibility values (~0.25 ± 0.02 SI), typically observed for gabbros, diorites, monzogranites, and granodiorites rocks. Differences can be seen at the edges, where the 2D magnetic model do not follow the clay pan geometry derived by TEM-1D models (Fig. 8g). This can be caused by a few circumstances: (1) Magnetics is known to be highly non-unique and the estimated magnetic susceptibility values may differ at depth and also along the profile; (2) The techniques are sensitive to different physical properties and have different resolution capabilities. The TEM method is sensitive in detecting conductive layers, but it loses resolution with depth especially for resistors. Despite the slight differences, the magnetic data can be fitted well and the 2D magnetic model is consistent and meaningful. The RMS between the observed and calculated magnetic data is 2.08 (Fig. 8f).

5. Integrated interpretation

The geophysical results presented in the previous sections were integrated into a conclusive interpretation of the subsurface structure of the Paranal site. In general, we observe a three-layer structure of the clay pan subsurface, with two prominent resistivity contrasts in the TEM-1D models. Whereas the upper resistivity contrast ~50 m is interpreted to display a lithological change in the sediment succession of the basin, the second resistivity contrast can be interpreted as the transition from the sediments to the resistive basement (Fig. 4). Please note that the derived TEM models are based on 1D inversion techniques. As discussed before, the general structure is well validated. However, 2D modeling studies along profile TC indicate that the depth of the basement is likely to be 20 m deeper than imaged by 1D. The data shed light on both the lithology and geometry (Fig. 9b and c) of the sediments infill as well as the structure of the basement rocks (Fig. 9a). Fig. 9d shows a summarizing sketch representing the Paranal clay pan.

5.1. Sedimentary lithology and basin geometry

Based on the TEM-derived resistivity models of the Paranal site, the basin is filled with an up to 160 ± 10 m-thick sediment succession above the basement contrast. Comparing the seismic profiles SA and SB with the derived TEM-1D models, a well-constrained resistivity and seismic velocity contrast at ~50 m depth is visible within the sediment sequence (Fig. 6). This two-layer structure of the sediment infill with a conductive strata below and a resistive layer above the transition strongly resembles the TEM data from the PAG site (Blanco et al., 2020). Taking also into account the similar formation of the two clay pans, a few although very careful assumptions about the sediment characteristics of the Paranal site can be transferred from PAG drill core (Fig. 7):

The upper and the lower sediment layer of the Paranal site derived by the TEM-1D models can presumably also be interpreted as colluvial and lacustrine sediments, respectively. Similar to PAG, the lower resistivity of the lacustrine sediments can likely be traced back to higher clay content, porosity, and/or compaction. Porosity differences of the sediment units might also explain the seismic velocity change at the colluvial/lacustrine transition derived from tomography results. The higher resistivity values of the lacustrine strata from Paranal compared to PAG, however, imply slight differences in the sediment characteristics, e.g., a lower clay-content, which might be caused by site-dependent catchment properties. The drainage catchment of the Paranal site is significantly smaller than the one of PAG, with higher slope angles and the surrounding alluvial fans being more proximal to the clay pan. The resulting shorter fluvial transport of sediment to the former lake likely caused a less efficient fluvial sorting and more disturbed/deteriorated lacustrine sediments. Furthermore, both sites are affected by different climatic conditions. The Paranal site, on the one hand, is placed outside of the hyperarid core of the Atacama Desert (<5 mm/yr MAP), and is thus influenced by more frequent rain events and even snow episodes due to its geographical location (higher in altitude and more distant to the coast). The PAG site, on the other hand, is located within the hyperarid core (<2 mm/yr MAP) but nearby the coast of the Pacific Ocean. Hence, the site is currently more affected by coastal fog (del Río et al., 2018; Walk et al., 2020), leading to a higher availability of dissolved ions (Diederich-Leicher, 2020; Dunai et al., 2020). Higher ion concentrations in the former lake periods, which are well documented in gypsum layers in the lacustrine strata (Diederich-Leicher, 2020), might

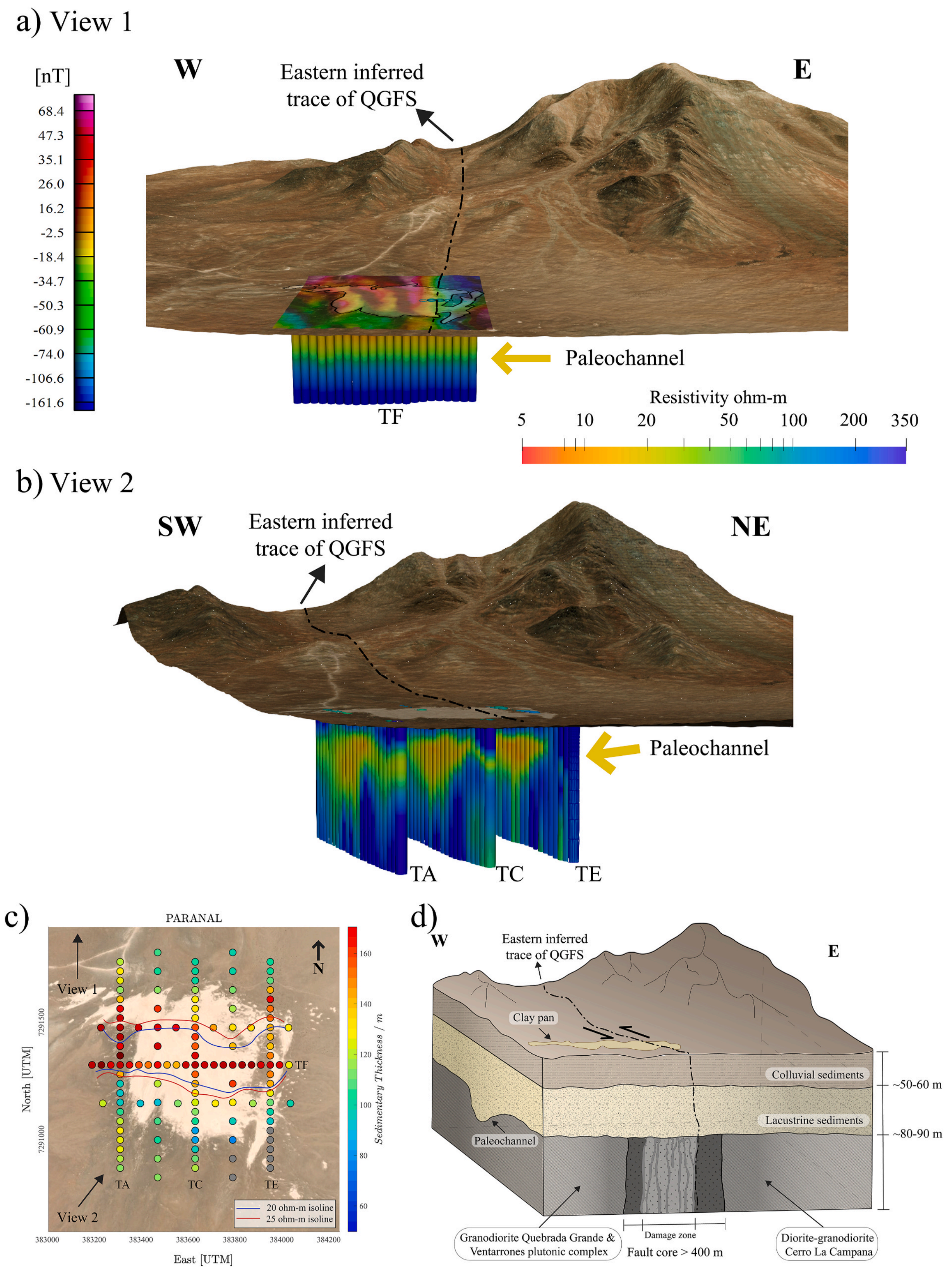

Fig. 9. 3D view of: (a) profile TF and (b) profiles TA, TC and TE based on the TEM-1D results based on OCR1 for Paranal site. For a plan view of the TEM profiles location refers to Fig. 1c. DEM obtained from (Kramm and Hoffmeister, 2021). Satellite image obtained from ESRI satellite image (ArcGIS, 2021). All TEM-1D models are shown up to 1900 m.a.s.l. The elevation is shown with double vertical exaggeration. Created in Paraview (Ahrens et al., 2005). (c) The sedimentary thickness of each station was derived by 1D inversion results using the MQ technique. Grey dots correspond to the stations where no conductive sediment layer was derived. Isolines of 20 and 25 Ω-m in blue and red color at 90 m depth. (d) Graphical illustration of the Paranal clay pan based on this work.

explain the higher electrical conductivity of the sediments.

As obvious in Fig. 7, both the colluvial and lacustrine sediments in Paranal are significantly thicker than in the PAG clay pan. Although no chronological information is available for the deeper sediments at both sites, the higher sediment thickness at Paranal might point to a higher sedimentation rate compared to PAG. This would be consistent with apparent hiatuses in the uppermost sediments from PAG, which illustrate phases of minor or lacking sediment accumulation (Ritter et al., 2018a). The higher sedimentation thickness is likely the result of more fluvial and surface runoff due to higher precipitation at Paranal as well as the less evolved gypsum cover in the catchment (Fernández-Martínez et al., 2019; Pfeiffer et al., 2021).

The shape of the conductive lacustrine sediments has an apparent west-east orientation (Fig. 9a and b). The sedimentary thickness is deepest across the profile TF and in the center of profile TC and varies between 100 and 170 m (Fig. 9c). Based on the derived TEM-1D models, we suggest that the initial lake formation took place in the former west-east orientated paleochannel as part of an old drainage system (Fig. 9d). Based on the orientation of the paleochannel, the sediment transportation could be mainly associated with the Vicuña Mackenna hill located to the northeast of the clay pan and currently the highest point at 3114 m.a.s.l. in the study zone.

Scheuber and Andriessen (1990) discuss the formation of the larger-scale Paranal drainage system to be at least of pre-late Miocene age (cf. Fig. 1a). However, the formation of the fault systems and the accumulation of the lacustrine sedimentary infill is expected to be much younger. Based on our geophysical results and the geological background of the site, the inferred paleochannel might be the main channel of the old drainage network that subsequently became abandoned due to tectonic blocking along the trace of the QGFS to the west of the clay pan. This outcome is relevant for understanding the old drainage network, also on a larger scale.

5.2. *Basement and fault system*

The resistivity values obtained for the third layer of the 1D models clearly indicate the presence of a resistive basement (>300 Ω-m). The Paranal clay pan covers plutonic complexes of different age, which are assumed to have similar lithologies based on their electrical properties. Our 2D magnetic modeling results indicates a third layer at approximately 90 m depth with high magnetic susceptibility that agrees with typical values for intrusive rocks as documented for Paranal catchment (Figs. 1b and 8g). The RAPS (Fig. 8d and e) point to shallow magnetic sources (at ~90 m depth) that are associated with the lacustrine sediments and a magnetic source at intermediate depth that is interpreted to be the basement (approximately ~140 m). The latter relates to the magnetic deposits beneath the sediments.

The analysis of the magnetic anomaly and the RTP response (Figs. 9a and 8b) visualize the spatial distribution of magnetic anomalies underneath the sediments. A significant change from northwest to southeast is observed. This change from positive to negative RTP response suggests a strong dependency on the existing basement units.

The large positive magnetic anomaly is associated with the Ventarrones plutonic complex and the Granodiorite Quebrada Grande to the northwest and, whereas the negative anomaly corresponds to the Diorite-granodiorite Cerro La Campana towards the east (Fig. 8a). The position of the magnetic anomaly change is consistent with the inferred eastern trace of the QGFS as visible in the geological map that cuts directly through the clay pan (Figs. 1b and 9a). The general structural geology of the strike-slip Atacama fault systems are well studied, with a fault core and a damaged zone leading to possible to higher porosity and metamorphosis/deterioration (Mitchell and Faulkner, 2009). The basement below the Paranal clay pan can thus be partly interpreted as a damaged zone of the strike-slip QGFS. The inferred eastern trace of the QGFS separates the Diorite-granodiorite Cerro La Campana to the east and the Granodiorite Quebrada Grande to the west (see in Fig. 1b). To confirm our findings and better delineate the magnetic anomalies on a local scale, a dense and extended magnetic survey covering the clay pan and the surroundings is required. Although aeromagnetic data is available on a regional scale, the resolution is not sufficient above the clay pan (SERNAGEOMIN, 2015b; 2015a).

6. Conclusions

The presented work illustrates the potential of an integrated geophysical study for a broad field of geological applications, such as paleoclimate investigations in desert environments. We investigated sedimentary deposits of the Paranal clay pan located in the arid core of the Atacama Desert using the Transient Electromagnetic method. In this case study, the loop source TEM method was complemented with magnetics and active seismics to resolve different subsurface properties at different spatial scales. A total amount of 116 TEM soundings were processed, analyzed, and inverted in order to investigate the resistivity distribution of the clay pan.

The 1D inversion results reveal that the clay pan can be interpreted by a three-layered resistivity structure with reliable information down to a depth of 250 m. The TEM-1D models yielded an upper layer of resistive colluvial sediments down to ~50 m depth, underlain by a second layer of conductive and presumably lacustrine sediments with a maximum sedimentary thickness of about 160 ± 10 m depth. The base of the sedimentary succession is formed by a third resistive basement layer with 400 Ω-m.

The comparison between the TEM-1D profiles and the tomography results is consistent with the transition depth between the different sediment strata. Two clusters are visible with a negative linear correlation leading to higher P wave velocities correlating with lower resistivities and vice versa.

The conductive body, associated to the lacustrine sediments, is distributed across a similar thickness in an east-west trend. The shape of the lacustrine sediments suggests the presence of an old paleochannel that might be part of the main old drainage system of the Paranal site.

The basement is also detected by the TEM method and is in well-agreement with the estimated magnetic sources depth by the RASP results and the 2D magnetic modeling. The magnetic results are consistent with the geological outcrop map, where the eastern inferred trace of the QGFS cuts directly through the clay pan. The analysis of magnetics reveals positive magnetic anomaly where Ventarrones plutonic complex and the Granodiorite Quebrada Grande is located. Therefore, the basement below the Paranal clay pan can be partly interpreted as a damaged zone of the strike slip QGFS. In addition, the 2D forward modeling study reveals 2D effects indicating that the basement depth of profile TC might be slightly deeper. The depth variation is around 24 m in the center of the clay pan, indicating a thicker conductive body of lacustrine sediments.

Interesting outcomes are observed from the PAG drill core information and the comparison with the 1D models of the Paranal site. The first resistivity and velocities layers are similar in both clay pans, suggesting colluvial sediments with similar electrical and mechanical properties. At the Paranal site, the transition zone from the colluvial to the lacustrine sediments is roughly 20 m deeper at the center of the clay pan. Moreover, the resistivity of lacustrine sediments at the Paranal site is increased by approximately ~20 Ω-m.

A high-resolution sedimentary geometry was derived covering the clay pan on a 3D grid. This study improves the understanding of sediment transportation in this hilly and arid environment exposed to different aridity, fluvial and pluvial periods. The derived 1D models are overall consistent, but slight underestimations arise for the depth of the basement. A 2D or even 3D inversion is required to resolve the clay pan's complex geometry for an unbiased and independent interpretation.

CRediT authorship contribution statement

B. Blanco-Arrué: Writing – review & editing, Writing – original draft, Visualization, Software, Validation, Data curation, Formal analysis, Investigation, Resources, Methodology, Conceptualization. **P. Yogeshwar:** Writing – review & editing, Writing – original draft, Visualization, Validation, Supervision, Software, Resources, Project administration, Methodology, Investigation, Formal analysis, Funding acquisition, Conceptualization. **B. Tezkan:** Funding acquisition, Conceptualization, Investigation, Project administration, Resources, Supervision, Writing – review & editing. **W. Mörbe:** Writing – review & editing, Methodology, Investigation. **D. Díaz:** Funding acquisition, Investigation, Project administration, Resources, Writing – review & editing. **B. Farah:** Writing – review & editing, Investigation, Formal analysis. **S. Buske:** Writing – review & editing, Investigation, Project administration, Resources, Validation. **L. Ninneman:** Writing – review & editing, Investigation, Formal analysis, Data curation. **J.P. Domagala:** Resources, Validation, Writing – review & editing. **J.L. Diederich-Leicher:** Writing – review & editing, Validation, Resources, Investigation. **A.C. Gebhardt:** Investigation, Resources, Validation, Writing – review & editing. **V. Wennrich:** Writing – review & editing, Visualization, Validation, Supervision, Resources, Project administration, Methodology, Investigation, Funding acquisition, Conceptualization.

Declaration of competing interest

The authors declare that they have no known competing financial interests or personal relationships that could have appeared to influence the work reported in this paper.

Acknowledgments

This project was funded by the Deutsche Forschungsgemeinschaft (DFG, German Research Foundation) – SFB-1211 – 268236062. B. Blanco-Arrué appreciates the support by the National Agency for Research and Development (ANID)/Scholarship Program/DOCTORADO BECAS CHILE-DAAD/2018 - 62170003. We acknowledge the support from DAAD (funding program number 57395809). We are grateful for all the support of the seismic equipment provided by the Geophysical Instrument Pool Potsdam. In addition, we appreciate the support of the magnetics and transient electromagnetic devices provided by the Department of Geophysics, University of Chile. We are thankful to all the people who collaborated with us for their support in the field and fruitful discussions during the preparation of this article. We are grateful the anonymous reviewers, and to the Editor-in-Chief A. Folguera, for constructive comments that greatly helped to improve the manuscript.

References

ABEM, 2016. Manual WalkTEM - Guideline Geo. Retrieved from. https://www.guidelinegeo.com/product/abem-walktem/.

Ahrens, J., Geveci, B., Law, C., 2005. Paraview: an end-user tool for large data visualization. In: The Visualization Handbook, p. 717.

Aina, A., 1986. Reduction to equator, reduction to pole and orthogonal reduction of magnetic profiles. Explor. Geophys. 17 (3), 141–145.

Allmendinger, R.W., González, G., Yu, J., Hoke, G., Isacks, B., 2005. Trench-parallel shortening in the northern Chilean forearc: tectonic and climatic implications. Geol. Soc. Am. Bull. 117 (1–2), 89–104.

Álvarez, F., Reich, M., Snyder, G., Pérez-Fodich, A., Muramatsu, Y., Daniele, L., Fehn, U., 2016. Iodine budget in surface waters from Atacama: natural and anthropogenic iodine sources revealed by halogen geochemistry and iodine-129 isotopes. Appl. Geochem. 68, 53–63.

ArcGIS, 2021. ESRI Satellite. Retrieved from. https://server.arcgisonline.com/ArcGIS/rest/services/World_Imagery/MapServer.

Bascuñán, S., Maksymowicz, A., Martínez, F., Becerra, J., Arriagada, C., Deckart, K., 2019. Geometry and late Mesozoic-Cenozoic evolution of the Salar de Atacama Basin (22° 30′-24° 30′ S) in the northern Central Andes: new constraints from geophysical, geochronological and field data. Tectonophysics 759, 58–78.

Blanco-Arrué, B., Yogeshwar, P., Tezkan, B., Díaz, D., 2021. Loop source transient electromagnetics in an urban noise environment: a case study in Santiago de Chile. Geophysics 86 (3), B135–B147.

Blanco, B., Yogeshwar, P., Tezkan, B., Wennrich, V., Buske, S., Ninnemann, L., Diaz, D., 2020. Investigation of sedimentary deposits in the Atacama desert-Chile using loop source transient electromagnetics. In: Paper presented at the 28. Schmucker-Weidelt-Kolloquium für Elektromagnetische Tiefenforschung. Haltern am See. https://gfzpublic.gfz-potsdam.de/pubman/item/item_5001615.

Brown, M., Diaz, F., Grocott, J., 1993. Displacement history of the Atacama fault system 25° 00′ S-27° 00′ S, northern Chile. Geol. Soc. Am. Bull. 105 (9), 1165–1174.

Bücker, M., Flores Orozco, A., Gallistl, J., Steiner, M., Aigner, L., Hoppenbrock, J., et al., 2021. Integrated land and water-borne geophysical surveys shed light on the sudden drying of large karst lakes in southern Mexico. Solid Earth 12 (2), 439–461.

Carrizo, D., González, G., Dunai, T., 2008. Constricción neógena en la Cordillera de la Costa, norte de Chile: neotectónica y datación de superficies con 21Ne cosmogónico. Rev. Geol. Chile 35 (1), 1–38.

Clark, D., Emerson, D., 1991. Notes on rock magnetization characteristics in applied geophysical studies. Explor. Geophys. 22 (3), 547–555.

Clarke, J.D., 2006. Antiquity of aridity in the Chilean Atacama desert. Geomorphology 73 (1–2), 101–114.

Coira, B., Davidson, J., Mpodozis, C., Ramos, V., 1982. Tectonic and magmatic evolution of the Andes of northern Argentina and Chile. Earth Sci. Rev. 18 (3–4), 303–332.

Constable, S.C., Parker, R.L., Constable, C.G., et al., 1987. Occam's inversion: A practical algorithm for generating smooth models from EM sounding data. Geophysics 52 (3), 289–300. https://doi.org/10.1190/1.1442303.

Cordell, D., Unsworth, M.J., Díaz, D., 2018. Imaging the Laguna del Maule Volcanic Field, central Chile using magnetotellurics: evidence for crustal melt regions laterally-offset from surface vents and lava flows. Earth Planet Sci. Lett. 488, 168–180.

Danielsen, J.E., Auken, E., Jørgensen, F., Søndergaard, V., Sørensen, K.I., 2003. The application of the transient electromagnetic method in hydrogeophysical surveys. J. Appl. Geophys. 53 (4), 181–198.

del Río, C., Garcia, J.-L., Osses, P., Zanetta, N., Lambert, F., Rivera, D., et al., 2018. ENSO influence on coastal fog-water yield in the Atacama Desert, Chile. Aerosol Air Qual. Res. 18 (1), 127–144.

DGAC, 2019. Reporte Climático. Retrieved from. https://climatologia.meteochile.gob.cl/application/publicaciones/reporteClimatologico/2019.

Díaz, D., Maksymowicz, A., Vargas, G., Vera, E., Contreras-Reyes, E., Rebolledo, S., 2014. Exploring the shallow structure of the San Ramón thrust fault in Santiago, Chile (∼ 33.5 S), using active seismic and electric methods. Solid Earth 5 (2), 837.

Diederich-Leicher, J.L., 2020. Climate History of the Hyperarid Core of the Atacama Desert Based on Clay pan Sediments. University of Cologne.

Diederich, J.L., Wennrich, V., Bao, R., Büttner, C., Bolten, A., Brill, D., et al., 2020. A 68 ka precipitation record from the hyperarid core of the Atacama Desert in northern Chile. Global Planet. Change 184, 103054.

Domagala, J., Escribano, J., De la Cruz, R., Saldías, J., Jorquera, R., 2016. Nos. 187-188, cartas blanco encalada y Pampa Remiendos, región de Antofagasta. Escala, 1: 100.000 [S. G. Básica].

Druskin, V., Knizhnerman, L., 1988. Spectral differential-difference method for numeric solution of three-dimensional nonstationary problems of electric prospecting. Izvestiya Earth Phys 24, 641–648.

Druskin, V., Knizhnerman, L., 1994. Spectral approach to solving three-dimensional Maxwell's diffusion equations in the time and frequency domains. Radio Sci. 29 (4), 937–953.

Druskin, V., Knizhnerman, L., Lee, P., 1999. New spectral Lanczos decomposition method for induction modeling in arbitrary 3-D geometry. Geophysics 64 (3), 701–706.

Dunai, T.J., López, G.A.G., Juez-Larré, J., 2005. Oligocene–Miocene age of aridity in the Atacama Desert revealed by exposure dating of erosion-sensitive landforms. Geology 33 (4), 321–324.

Dunai, T.J., Melles, M., Quandt, D., Knief, C., Amelung, W., 2020. Whitepaper: earth–evolution at the dry limit. Global Planet. Change, 103275.

Fernández-Martínez, M.Á., dos Santos Severino, R., Moreno-Paz, M., Gallardo-Carreño, I., Blanco, Y., Warren-Rhodes, K., et al., 2019. Prokaryotic community structure and metabolisms in shallow subsurface of Atacama Desert playas and alluvial fans after heavy rains: repairing and preparing for next dry period. Front. Microbiol. 10, 1641.

Fitterman, D.V., Stewart, M.T., 1986. Transient electromagnetic sounding for groundwater. Geophysics 51 (4), 995–1005.

Frei, W., Keller, L., 2000. Hybride Seismik—eine verbesserte Methode des Aussagepotentials seismischer Daten [Hybrid seismic surveying—a method to better view the information content in seismic data]. Bull. Angew Geol. Bull. Appl. Geol. 5 (2), 229–236.

Frischknecht, F.C., Raab, P., 1984. Time-domain electromagnetic soundings at the Nevada test site, Nevada. Geophysics 49 (7), 981–992.

García-Pérez, T., Marquardt, C., Yáñez, G., Cembrano, J., Gomila, R., Santibañez, I., Maringue, J., 2018. Insights on the structural control of a Neogene forearc basin in Northern Chile: a geophysical approach. Tectonophysics 736, 1–14.

Goldman, M., Neubauer, F., 1994. Groundwater exploration using integrated geophysical techniques. Surv. Geophys. 15 (3), 331–361.

Hartley, A.J., Chong, G., 2002. Late Pliocene age for the Atacama desert: implications for the desertification of western south America. Geology 30 (1), 43–46.

Hartley, A.J., Chong, G., Houston, J., Mather, A.E., 2005. 150 million years of climatic stability: evidence from the Atacama Desert, northern Chile. J. Geol. Soc. 162 (3), 421–424.

Herve, M., 1987. Movimiento normal de la falla Paposo, Zona de Falla Atacama, en el Mioceno, Chile. Andean Geol. 31, 31–36.

Herve, M., Marinovic, N., 1989. Geocronología y evolución del Batolito Vicuña Mackenna, Cordillera de la Costa, sur de Antofagasta (24-25 S). Andean Geol. 16 (1), 31–49.

Hoffmann-Rothe, A., Ritter, O., Janssen, C., 2004. Correlation of electrical conductivity and structural damage at a major strike-slip fault in northern Chile. J. Geophys. Res. Solid Earth 109 (B10).

Hördt, A., Druskin, V.L., Knizhnerman, L.A., Strack, K.-M., 1992. Interpretation of 3-D effects in long-offset transient electromagnetic (LOTEM) soundings in the Münsterland area/Germany. Geophysics 57 (9), 1127–1137.

Houston, J., Hartley, A.J., 2003. The central Andean west-slope rainshadow and its potential contribution to the origin of hyper-aridity in the Atacama Desert. Int. J. Climatol.: A Journal of the Royal Meteorological Society 23 (12), 1453–1464.

Ibraheem, I.M., Gurk, M., Tougiannidis, N., Tezkan, B., 2018. Subsurface investigation of the Neogene Mygdonian Basin, Greece using magnetic data. Pure Appl. Geophys. 175 (8), 2955–2973.

Ishihara, S., Ulriksen, C.E., 1980. The magnetite-series and ilmenite-series granitoids in Chile. Min. Geol. 30 (161), 183–190.

Kramm, T., Hoffmeister, D., 2021. High resolution digital elevation model (Paranal Claypan area). from CRC1211 Database. https://www.crc1211db.uni-koeln.de/search/view.php?dataID=415.

Marinovic, N., Smoje, I., Maksaev, V., Hervé, M., Mpodozis, C., 1995. Hoja Aguas Blancas, Región de Antofagasta, Carta Geológica de Chile N 70, escala 1: 250.000. Servicio Nacional de Geología y Minería, Santiago.

Marson, I., Klingele, E., 1993. Advantages of using the vertical gradient of gravity for 3-D interpretation. Geophysics 58 (11), 1588–1595.

Martin, R., 2009. Development and Application of 2D and 3D Transient Electromagnetic Inverse Solutions Based on Adjoint Green Functions: A Feasibility Study for the Spatial Reconstruction of Conductivity Distributions by Means of Sensitivities. Universität zu Köln.

Meju, M.A., 1998. A simple method of transient electromagnetic data analysis. Geophysics 63 (2), 405–410.

Menke, W., 2018. Geophysical Data Analysis: Discrete Inverse Theory. Academic press.

Mitchell, T., Faulkner, D., 2009. The nature and origin of off-fault damage surrounding strike-slip fault zones with a wide range of displacements: a field study from the Atacama fault system, northern Chile. J. Struct. Geol. 31 (8), 802–816.

Montecinos-Cuadros, D., Díaz, D., Yogeshwar, P., Munoz-Saez, C., 2021. Characterization of the shallow structure of El Tatio geothermal field in the Central Andes, Chile using transient electromagnetics. J. Volcanol. Geoth. Res. 412, 107198.

Mpodozis, C., Ramos, V., 1990. The Andes of Chile and Argentina.

Nabighian, M.N., Macnae, J.C., 1991. Time domain electromagnetic prospecting methods. Electromagnetic methods in applied geophysics 2, 427–509.

NASA, 2020. NASADEM Merged DEM Global 1 Arc Second V001. https://doi.org/10.5067/MEaSUREs/NASADEM/NASADEM_HGT.001. Retrieved from.

Ninnemann, L., 2020. *Seismische Abbildung der Struktur dreier Tonpfannen in der Atacama-Wüste mit Hilfe von Ersteinsatz-Laufzeittomographie.* (Bachelor). Institute of Geophysics and Geoinformatics, TU Bergakademie Freiberg. Freiberg, Germany. (Matrikel: 61 235).

Pardo-Casas, F., Molnar, P., 1987. Relative motion of the Nazca (farallon) and south American plates since late cretaceous time. Tectonics 6 (3), 233–248.

Pearson, K., 1895. VII. Note on regression and inheritance in the case of two parents. In: Proceedings of the royal society of London, 58. Royal Society, pp. 240–242.

Pfeiffer, M., Morgan, A., Heimsath, A., Jordan, T., Howard, A., Amundson, R., 2021. Century scale rainfall in the absolute Atacama Desert: landscape response and implications for past and future rainfall. Quat. Sci. Rev. 254, 106797.

Phillips, R.J., Zuber, M.T., Solomon, S.C., Golombek, M.P., Jakosky, B.M., Banerdt, W.B., et al., 2001. Ancient geodynamics and global-scale hydrology on Mars. Science 291 (5513), 2587–2591.

Rajagopalan, S., 2003. Analytic signal vs. reduction to pole: solutions for low magnetic latitudes. Explor. Geophys. 34 (4), 257–262.

Reyes-Wagner, V., Díaz, D., Cordell, D., Unsworth, M., 2017. Regional electrical structure of the Andean subduction zone in central Chile (35–36 S) using magnetotellurics. Earth Planets Space 69 (1), 1–9.

Ritter, B., Binnie, S.A., Stuart, F.M., Wennrich, V., Dunai, T.J., 2018a. Evidence for multiple Plio-Pleistocene lake episodes in the hyperarid Atacama Desert. Quat. Geochronol. 44, 1–12.

Ritter, B., Stuart, F.M., Binnie, S.A., Gerdes, A., Wennrich, V., Dunai, T.J., 2018b. Neogene fluvial landscape evolution in the hyperarid core of the Atacama Desert. Sci. Rep. 8 (1), 1–16.

Ritter, B., Wennrich, V., Medialdea, A., Brill, D., King, G., Schneiderwind, S., et al., 2019. Climatic fluctuations in the hyperarid core of the Atacama Desert during the past 215 ka. Sci. Rep. 9 (1), 1–13.

Rödder, A., Tezkan, B., 2013. A 3D resistivity model derived from the transient electromagnetic data observed on the Araba fault, Jordan. J. Appl. Geophys. 88, 42–51.

Roest, W.R., Verhoef, J., Pilkington, M., 1992. Magnetic interpretation using the 3-D analytic signal. Geophysics 57 (1), 116–125.

Scheuber, E., Andriessen, P.A., 1990. The kinematic and geodynamic significance of the Atacama fault zone, northern Chile. J. Struct. Geol. 12 (2), 243–257.

Scholl, C., 2005. The influence of multidimensional structures on the interpretation of LOTEM data with one-dimensional models and the application to data from Israel. Ph.D. thesis. Universität zu Köln, Institut für Geophysik und Meteorologie. URL: https://kups.ub.uni-koeln.de/1597/.

SEEQUENT, 2021. Oasis montaj. Retrieved from. https://www.seequent.com/products-solutions/geosoft-oasis-montaj/.

SERNAGEOMIN, 2015a. Carta magnética blanco encalada y Pampa Remiendos, región de Antofagasta. Escala, 1:100.000 [S. G. Básica].

SERNAGEOMIN, 2015b. Carta magnética punta posallaves y Sierra Vicuña Mackenna, región de Antofagasta. Escala, 1:100.000 [S. G. Básica].

Skarmeta, J., Marinovic, N., 1981. Geología de la Hoja quillagua. Región de Antofagasta. Escala, 1: 250.000.

Ślęzak, K., Díaz, D., Vargas, J.A., Cordell, D., Reyes-Cordova, F., Segovia, M.J., 2021. Magnetotelluric image of the Chilean subduction zone in the Salar de Atacama region (23°-24° S): insights into factors controlling the distribution of volcanic arc magmatism. Phys. Earth Planet. In. 106765.

Solomon, S., Aharonson, O., Aurnou, J., Banerdt, W., Carr, M., Dombard, A., et al., 2005. New perspectives on ancient Mars. Science 307, 1214–1220.

Spector, A., Grant, F., 1970. Statistical models for interpreting aeromagnetic data. Geophysics 35 (2), 293–302.

Spies, B.R., 1989. Depth of investigation in electromagnetic sounding methods. Geophysics 54 (7), 872–888.

Sudha, K., Tezkan, B., Israil, M., Rai, J., 2011. Combined electrical and electromagnetic imaging of hot fluids within fractured rock in rugged Himalayan terrain. J. Appl. Geophys. 74 (4), 205–214.

Talwani, M., 1964. Computation of magnetic anomalies caused by two-dimensional bodies of arbitrary shape. Computers in the mineral industries 1, 464–480.

Ugalde, H., Valenzuela, M., Milkereit, B., 2007. An integrated geophysical and geological study of the Monturaqui impact crater, Chile. Meteoritics Planet Sci. 42 (12), 2153–2163.

Walk, J., Stauch, G., Reyers, M., Vásquez, P., Sepúlveda, F.A., Bartz, M., et al., 2020. Gradients in climate, geology, and topography affecting coastal alluvial fan morphodynamics in hyperarid regions–the Atacama perspective. Global Planet. Change 185, 102994.

Ward, S.H., Hohmann, G.W., 1988. Electromagnetic theory for geophysical applications. In: Electromagnetic Methods in Applied Geophysics: Voume 1, Theory. Society of Exploration Geophysicists, pp. 130–311.

Won, I., Bevis, M., 1987. Computing the gravitational and magnetic anomalies due to a polygon: algorithms and Fortran subroutines. Geophysics 52 (2), 232–238.

Yáñez, G., Perez-Estay, N., Araya-Vargas, J., Sanhueza, J., Figueroa, R., Maringue, J., Rojas, T., 2020. Shallow anatomy of the San Ramón Fault (Chile) constrained by geophysical methods: implications for its role in the Andean deformation. Tectonics 39 (8), e2020TC006294.

Yogeshwar, P., Küpper, M., Tezkan, B., Rath, V., Kiyan, D., Byrdina, S., et al., 2020. Innovative boat-towed transient electromagnetics — investigation of the Furnas volcanic lake hydrothermal system, Azores. Geophysics 85 (2), E41–E56. https://doi.org/10.1190/geo2019-0292.1.

Yogeshwar, P., Tezkan, B., 2018. Analysing two-dimensional effects in central loop transient electromagnetic sounding data using a semi-synthetic tipper approach. Geophys. Prospect. 66 (2), 444–456.

Yogeshwar, P., Tezkan, B., Haroon, A., 2013. Investigation of the Azraq sedimentary basin, Jordan using integrated geoelectrical and electromagnetic techniques. Near Surf. Geophys. 11 (4), 381–390.

Zhang, J., Toksöz, M.N., 1998. Nonlinear refraction traveltime tomography. Geophysics 63 (5), 1726–1737.